Heliyon 10 (2024) e27571

Contents lists available at ScienceDirect

Heliyon

journal homepage: www.cell.com/heliyon

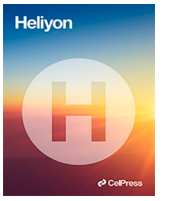

Research article

FTO-mediated autophagy inhibition promotes non-small cell lung cancer progression by reducing the stability of SESN2 mRNA

Kai Wang [a,1], Zhiqiang Mei [a,1], Meiling Zheng [a], Xiaoyan Liu [a], Dabing Li [b,**], Haiyong Wang [c,*]

[a] *Key Laboratory of Epigenetics and Oncology, Research Center for Preclinical Medicine, Southwest Medical University, Luzhou, 646000, China*
[b] *School of Basic Medical Sciences, Southwest Medical University, Luzhou, 646000, China*
[c] *Department of Internal Medicine Oncology, Shandong Cancer Hospital and Institute, Shandong First Medical University and Shandong Academy of Medical Sciences, Jinan, 250117, China*

ARTICLE INFO

Keywords:
FTO
SESN2
Autophagic flux
mRNA stability
Lung cancer

ABSTRACT

The role of fat mass and obesity-associated protein (FTO), an N^6-methyladenosine (m^6A) demethylase, in non-small cell lung cancer (NSCLC) has recently received widespread attention. However the underlying mechanisms of FTO-mediated autophagy regulation in NSCLC progression remain elusive. In this study, we found that *FTO* was significantly upregulated in NSCLC, and downregulation of *FTO* suppressed the growth, invasion and migration of NSCLC cells by inducing autophagy. *FTO* knockdown resulted in elevated m^6A levels in NSCLC cells. Methylated RNA immunoprecipitation sequencing showed that sestrin 2 (SESN2) was involved in m^6A regulation during autophagy in NSCLC cells. Interestingly, m^6A modifications in exon 9 of *SESN2* regulated its stability. *FTO* deficiency promoted the binding of insulin-like growth factor 2 mRNA-binding protein 1 to *SESN2* mRNA, enhancing its stability and elevating its protein expression. FTO inhibited autophagic flux by downregulating *SESN2*, thereby promoting the growth, invasion and migration of NSCLC cells. Besides, the mechanism by which FTO blocked SESN2-mediated autophagy activation was associated with the AMPK-mTOR signaling pathway. Taken together, these findings uncover an essential role of the FTO–autophagy–SESN2 axis in NSCLC progression.

1. Introduction

Lung cancer has the highest mortality rate worldwide among all the malignancies [1]. Despite significant advances in comprehensive treatment strategies for lung cancer [2,3], the five-year survival rate remains low due to high recurrence and metastasis [4]. Non-small cell lung cancer (NSCLC) accounts for about 80–90% of all lung cancer cases, and approximately 30% of NSCLC patients exhibit concomitant lymph node metastases upon diagnosis [5]. In the United States, 55% of patients newly diagnosed with NSCLC display distant metastases, which account for nearly 90% of patient deaths [6]. Therefore, elucidating the molecular mechanisms underlying the malignant progression and metastasis of NSCLC is essential for developing rational and targeted interventions that can improve patient survival.

* Corresponding author.
** Corresponding author.
E-mail addresses: lidabing@swmu.edu.cn (D. Li), wanghaiyong6688@126.com (H. Wang).
[1] These authors contributed equally to this work.

https://doi.org/10.1016/j.heliyon.2024.e27571
Received 22 October 2023; Received in revised form 29 February 2024; Accepted 1 March 2024
Available online 7 March 2024
2405-8440/© 2024 Published by Elsevier Ltd. This is an open access article under the CC BY-NC-ND license (http://creativecommons.org/licenses/by-nc-nd/4.0/).

Being the most abundant mRNA modification in eukaryotes, N^6-methyladenosine (m^6A) is involved in the metabolism of multiple RNAs (mRNAs, micro RNAs, long noncoding RNAs) and plays a critical role in various diseases, such as cancer [7], obesity [8,9], atherosclerosis [10], pulmonary hypertension [10], heart disease [11], Alzheimer's disease [12]. m^6A modifications affect mRNA degradation, translation, subcellular localization, and alternative splicing by regulating the 5'cap, 3'untranslated region (UTR), and RNA termination codon [13–15]. This RNA modification is modulated by three critical moieties: "readers" (methyl-specific binding proteins), "erasers" (m^6A demethylases), and "writers" (m^6A methyltransferases) [13–15].

Fat mass and obesity-associated protein (FTO) functions as an m^6A demethylase that is essential for mRNA processing. FTO is highly expressed in lung cancer tissues and is associated with low patient survival [16]. FTO was also found to promote the proliferation, invasion, and migration of the lung cancer cell lines A549 and H1299 [17]. Mechanistically, FTO exerts tumor-promoting effects by reducing the levels of m^6A and enhancing the mRNA stability of *MZF1* and *USP7* [16,18]. However, the role of FTO in regulating autophagy is controversial.

Autophagy is a highly conserved cellular self-protective mechanism that aims to satisfy the metabolic requirements of cells under unfavorable conditions (e.g., nutritional deficiency and hypoxia) by degrading cargoes like misfolded proteins and nucleic acids [19]. Autophagy is closely related to tumor formation and development [20] and hinders tumor progression and metastasis [21–24]. FTO was shown to inhibit autophagic flux in mouse embryonic fibroblasts by activating the mammalian target of rapamycin complex 1 pathway [25]. Knockdown of FTO activated autophagic flux and suppressed tumorigenesis [23,24]. Conversely, FTO was shown to induce autophagy by upregulating Unc-51-like autophagy-activating kinase 1 [26]. Upon deleting the gene encoding FTO, *Atg5* and *Atg7* mRNAs were m^6A-modified, allowing YTHDF2 to bind to them and ultimately affect the assembly of autophagic vesicles [27]. The mechanism by which FTO-mediated autophagy inhibition supports the malignant progression of NSCLC is currently unclear.

In the present study, we demonstrate for the first time that sestrin 2 (SESN2) is involved in regulating m^6A modifications during autophagy in NSCLC cells. Furthermore, FTO-mediated autophagy inhibition facilitates the malignant progression of NSCLC by reducing the mRNA stability of *SESN2*.

2. Materials and methods

2.1. NSCLC patient samples and cell culture

NSCLC tissues (n = 10) and adjacent normal tissues (n = 10) were obtained from NSCLC patients treated at Shandong Cancer Hospital and immediately stored at −80 °C for total RNA or protein extraction in the future. Informed consent was solicited from the patients before starting this study. These samples were obtained with the approval of the Ethics Committee of Shandong Cancer Hospital and Institute (SDZLEX2021-054-01). This study was conducted in accordance with the Declaration of Helsinki. The human NSCLC cell lines H1975, PC9, H460, A549, and H1299 and the lung epithelial cell line BEAS-2R were acquired from the American Type Culture Collection (VA, USA) and routinely cultured in RPMI 1640 medium containing 1% streptomycin/penicillin and 10% fetal bovine serum in an incubator with 5% CO_2. 3-Methyladenine (3 MA; Sigma-Aldrich, MO, USA) and rapamycin (Beyotime, Nanjing, China) were prepared at final concentrations of 1 mM and 100 nM to inhibit and induce autophagic flux in NSCLC cells, respectively.

2.2. Reverse transcription-PCR (RT–PCR)

RT–PCR was carried out as previously described [28]. Briefly, total RNA was extracted from H460 and H1975 cells and frozen tissues using the Ultrapure Total RNA Extraction kit (Simgen, Hangzhou, China), reverse-transcribed into cDNA (TIANGEN, Beijing, China), and subjected to RT–PCR using PCR Taq Master Mix (TIANGEN, Beijing, China) and relevant primers. *ACTB* served as an internal reference to normalize gene expression. The following primers were used for RT–PCR: *FTO*: Forward 5′-ACCCCTTCACCAAGGAGACT-3′, Reverse 5′-CATTCTGCAGAGCCAACTGA-3'; *SESN2*: Forward 5′-AGAGGGCACAGGAAAGAA-3′, Reverse 5′-TCAAGCATAAAGGACCAAA-3'; *ACTB*: Forward 5′-CTGAAGTACCCCATCGAGCA-3′, Reverse 5′-CCACTCACCTGGGTCATCTT-3'.

Table 1
Primary and secondary antibodies.

Primary antibodies	Antibody dilutions	Manufacturer, Country, Catalogue number
Rabbit anti-LC3B antibody	1:1000	Cell Signaling Technology, USA, 3868S
Rabbit anti-FTO antibody	1:2000	Proteintech, USA, 27226-1-AP
Rabbit anti-IGF2BP1 antibody	2 μg for 2.5 mg of total protein lysate	Proteintech, USA, 22803-1-AP
Mouse anti-Sestrin 2 antibody	1:1000	Proteintech, USA, 66297-1-Ig
Mouse anti-SQSTM1/p62 antibody	1:400	Cell Signaling Technology, USA, 88588S
Mouse anti-phospho-mTOR (Ser2448) antibody	1:2000	Proteintech, USA, 67778-1-Ig
Rabbit anti-mTOR antibody	1:2000	Proteintech, USA, 28273-1-AP
Rabbit anti-phospho-AMPK alpha (Thr172) antibody	1:1000	Affinity Biosciences, USA, AF3423
Rabbit anti-AMPK alpha antibody	1:3000	Proteintech, USA, 10929-2-AP
Rabbit anti-GAPDH antibody	1:10000	Proteintech, USA, 10494-1-AP
Goat Anti-Mouse IgG H&L (Alexa Fluor 647)	1:500	Abcam, USA, ab150115
HRP-labeled Goat Anti-Rabbit IgG(H + L)	1:1000	Beyotime, China, A0208
HRP-labeled Goat Anti-Mouse IgG(H + L)	1:1000	Beyotime, China, A0216

2.3. Total m^6A quantification

Total m^6A levels in tissues and cells were determined using the EpiQuik™ m^6A RNA Methylation Quantification Kit (Colorimetric), according to the manufacturer's instructions. Briefly, 200 ng of the isolated total RNA was added to assay wells, followed by the relevant antibody diluent at an appropriate concentration for m^6A RNA capture. Finally, Developer and Stop solutions were added sequentially to each well and incubated for 10min under light. After the solutions turned yellow, their absorbance was measured at 450 nm using the MultiskanGO microplate photometer (Thermo Scientific, Carthage, MO, USA). The m^6A levels were calculated using the following formula: $m6A\ (\%) = [(Sample_{OD} - NC_{OD})/S]/[(PC_{OD} - NC_{OD})/P] \times 100\%$, where S denotes the amount of sample RNA (ng), P denotes the amount of positive control RNA (ng), NC denotes negative control, PC denotes positive control, and OD denotes optical density. All primary and secondary antibodies used are listed in Table 1.

2.4. Plasmids and transfection

EGFP-LC3b and SESN2 plasmids were constructed by Changsha Fenghui and Guangzhou iGene, respectively. The RFP-GFP-LC3 lentiviral vector was purchased from HANBIO Co., Ltd (Shanghai). Synthetic lentiviral short hairpin RNA (shRNA) oligonucleotides (SyngenTech, Beijing, China) was utilized to target and silence *FTO* expression. Puromycin was used to screen stable cell lines harboring *FTO* knockdown for animal experiments. Different small interfering RNAs (siRNAs; Beijing Tsingke Biotech Co., Ltd., Beijing, China) were used to knock down *FTO* and *IGF2BP1*, and the best-performing sequences were selected for *in vitro* experiments. In addition, the cDNA sequences of the genes encoding wild-type and mutant FTO and wild-type and mutant SESN2 were cloned into pcDNA3.1 (BINGENE, Beijing, China), as previously described [24,27,29]. Plasmid and siRNA transfections were performed using a Lipofectamine™ 2000 reagent, as previously described [30]. All siRNA sequences and shRNA lentiviral vectors are listed in Table 2.

2.5. Western blotting

NSCLC cells were lysed in cold protein lysis buffer for 20min, as previously described [22,30]. After quantifying total protein concentrations, the lysates were separated by sodium dodecyl sulfate–polyacrylamide gel electrophoresis on 12.5% gels and transferred at 100 V for 2 h onto methanol-activated polyvinylidene fluoride membranes, which were blocked with 5% skimmed milk and incubated with primary and secondary antibodies. Relevant protein bands were visualized using the G: BOX Imaging System (Syngene, Cambridge, UK) and quantified using ImageJ (NIH, USA).

2.6. Immunofluorescence

Tissue sections from the xenograft mouse model and NSCLC cell lines were antigenically repaired, blocked with normal goat serum, and incubated overnight at 4 °C with anti-SESN2/anti-SQSTM1/p62 primary antibody and goat anti-mouse IgG H&L (Alexa Fluor 647) antibody. The fluorescence signal of SESN2/p62 was captured using the ApoTome imaging system (ZEISS, Shanghai, China).

2.7. Immunohistochemistry

After being deparaffinized and antigenically repaired, pathological sections of human NSCLC tissues and adjacent normal tissues were subsequently blocked with normal goat serum, incubated with anti-FTO primary antibody and HRP-labeled goat anti-rabbit IgG (H + L), and subjected to a color reaction using the 3, 3N-Diaminobenzidine Tertrahydrochloride Horseradish Peroxidase Chromogenic Kit (Beyotime, Nanjing, China). The integrated optical density of FTO was quantified using ImageJ.

Table 2
Description of siRNA sequences and shRNA lentiviral vectors.

Sequences of siRNAs	
Negative control (siCtrl)	Sense: 5′-UUCUCCGAACGUGUCACGUTT-3′; Antisense: 5′-ACGUGACAGGUUCGGAGAATT-3′
siFTO#1	Sense: 5′-GUUCAAGAAGCCUUUCUCA-3′; Antisense: 5′-UGAGAAAGGCUUCUUGAAC-3′
siFTO#2	Sense: 5′-CCUACAACGGACAAGAUGA-3′; Antisense: 5′-UCAUCUUGUCCGUUGUAGG-3′
siFTO#3	Sense: 5′-GCUAUUUCAUGCUUGAUGA-3′; Antisense: 5′-UCAUCAAGCAUGAAAUAGC-3′
siIGF2BP1	Sense: 5′-GGUUCAGAGUGAAGAAGUAAC-3′; Antisense: 5′-UACUUCUUCACUCUGAACCUU-3′
shRNA lentiviral vectors	
shCtrl	pLV-hU6-NC shRNA03-hef1a-mNeongreen-P2A-Puro
shFTO	pLV-hU6-FTO-shRNA02(Human)-hef1a-mNeongreen-P2A-Puro

2.8. Cell viability

Cell viability was measured as previously described [30]. *FTO*-knockdown NSCLC cells were seeded in 96-well plates, treated with 1 mM 3 MA for 48 h, and incubated with 3-(4, 5-dimethylthiazol-2-yl)-2, 5-diphenyltetrazolium bromide (MTT) solution for 4 h. The reaction was terminated using dimethyl sulfoxide, and absorbance was measured at 570 nm using the Multiskan GO microplate photometer.

2.9. Autophagy detection by fluorescence imaging analysis

For microscopy analysis of EGFP-LC3b fluorescence, we examined the subcellular localization of autophagosomes using EGFP-LC3b-expressing cells. As the EGFP-LC3b fusion protein can be transferred to the autophagosome membrane during autophagy and form a number of green fluorescent punctate dots under the fluorescence microscope. Briefly, EGFP-LC3b plasmid was transfected into H460 and H1975 cells with the Lipofectamine™ 2000 reagent. Stable transfected cells expressing EGFP-LC3b were obtained after two weeks of screening these cells with distinct concentrations of G418 (100–1000 μg/mL). EGFP-LC3b punctate dots% = EGFP-LC3b punctate cells/positive cells [22,30], three fields per group were randomly counted.

For microscopy analysis of RFP-GFP-LC3 fluorescence, we determined the subcellular localization of autophagosomes/autolysosomes using RFP-GFP-LC3-expressing cells. RFP-GFP-LC3 has been shown to accurately detect autophagy flux [31]. Under acidic conditions (pH $<$ 5.5), RFP fluorescence is stable, while GFP fluorescence can be quenched. When RFP-GFP-LC3 fusion protein is transferred to autophagosomes (pH $\approx$ 7), RFP-GFP-LC3 shows green and red fluorescent dots, and the yellow fluorescent co-localized dots represent autophagosomes. Once autophagosomes fuse with lysosomes to form autolysosomes, the acidic environment in the lumen of the autolysosomes enables GFP fluorescence to be quenched, whereas RFP is not. Thus, the red fluorescent co-localized dots indicate autolysosomes. In this study, siFTO#1, siFTO#2, and siFTO#3 were transiently transfected into H460 and H1975 cells stably expressing RFP-GFP-LC3 for 24h. Then, yellow/red fluorescent co-localized dots in control and *FTO*-knockdown cells were detected using the ApoTome imaging system (Zeiss, Shanghai, China). Three fields per group were randomly counted. Quantification of autophagosomes/autolysosomes was presented as the mean of the number of autophagosomes/autolysosomes in cells per unit area.

2.10. Transmission electron microscopy

NSCLC cells were fixed in 2.5% glutaraldehyde solution at 4 °C for 4 h, washed with phosphate-buffered saline, fixed in 1% osmium acid for 2h, dehydrated using acetone, and embedded in a permeable resin to make ultrarapid sections, which were stained with lead nitrate and observed under a transmission electron microscope (Hitachi, Shanghai, China) to study the ultrastructure of autophagosomes and autolysosomes. Autophagosomes are double-membrane vesicular structures, whereas autolysosomes are single-membrane structures containing mostly degraded cytoplasmic components such as endoplasmic reticulum, mitochondria, and ribosomes. Three fields per group were randomly counted.

2.11. Cell invasion and migration assays

NSCLC cells were seeded in the upper Transwell chambers (Corning, USA), which were precoated with or without 0.4 mg/mL Matrigel (BD Biosciences, USA), and incubated in serum-free RPMI-1640 medium. The lower chambers were filled with RPMI 1640 medium containing 10% fetal bovine serum. After 48h, the cells on the lower surface of the chambers were fixed in 4% paraformaldehyde, stained with crystal violet for 25min, and counted under a microscope. Three fields per chamber were randomly counted.

2.12. Luciferase reporter assay

NSCLC cells (2×10^6) were seeded in 60 mm dishes, transfected with plasmids encoding wild-type or mutant SESN2 for 24 h, re-seeded in 96-well plates, and subjected to luciferase reporter assay (RG028, Beyotime, Nanjing, China) using the SpectraMax M5 multifunction microplate reader (Molecular Devices, USA). Briefly, cell supernatants were collected after cell lysis. Firefly and Renilla luciferase reagents were sequentially added to 100 μL of each supernatant, and activation of the target reporter genes was evaluated based on the relative light unit ratios of Firefly to Renilla luciferase.

2.13. RNA stability

NSCLC cells were treated with 5 μg/mL actinomycin D (ActD) for 0–12h to block mRNA transcription. Subsequently, total RNA was extracted to measure the target mRNA levels using RT-PCR.

2.14. Methylated RNA immunoprecipitation sequencing (MeRIP-seq)

MeRIP-seq was outsourced to CLOUDSEQ (Shanghai, China). Total RNA was extracted from H460 cells treated with or without 100 nM rapamycin and subjected to quality control. These RNAs were randomly fragmented into about 200 nt fragments. The RNA fragments were then incubated with m^6A antibody conjugated to Protein A/G magnetic beads at 4 °C for 4h to allow full binding. The

supernatant containing m^{6}A RNA was then collected with m^{6}A competitive eluting fluids and purified with phenol: chloroform: isoamyl alcohol (125:24:1). RNA sequencing libraries were constructed using the GenSeq Low Input Whole RNA Library Prep kit (GenSeq, Inc.) [32,33]. A portion of the RNA was subsequently analyzed by high-throughput sequencing using the NovaSeq platform (Illumina), while the remaining RNA was reverse transcribed for subsequent experiments. The MeRIP-seq data is available at Gene Expression Omnibus under the accession number GSE240879. The datasets analyzed during the current study are available from the corresponding author upon reasonable request.

2.15. RIP–quantitative PCR (qPCR)

NSCLC cell supernatants were obtained by lysing the cells in ice-cold RIP lysis buffer for 30 min and centrifuging the lysates at 12000 rpm. Magnetic beads were conjugated to anti-IGF2BP1 antibody using the Magna RIP RNA Binding Protein Immunoprecipitation Kit (Sigma-Aldrich, USA) and incubated overnight with the cell supernatants at 4 °C. Unbound material was washed away, and the RNA bound to anti-IGF2BP1 antibody was purified, reverse transcribed into cDNA, and subjected to qPCR as previously described [34].

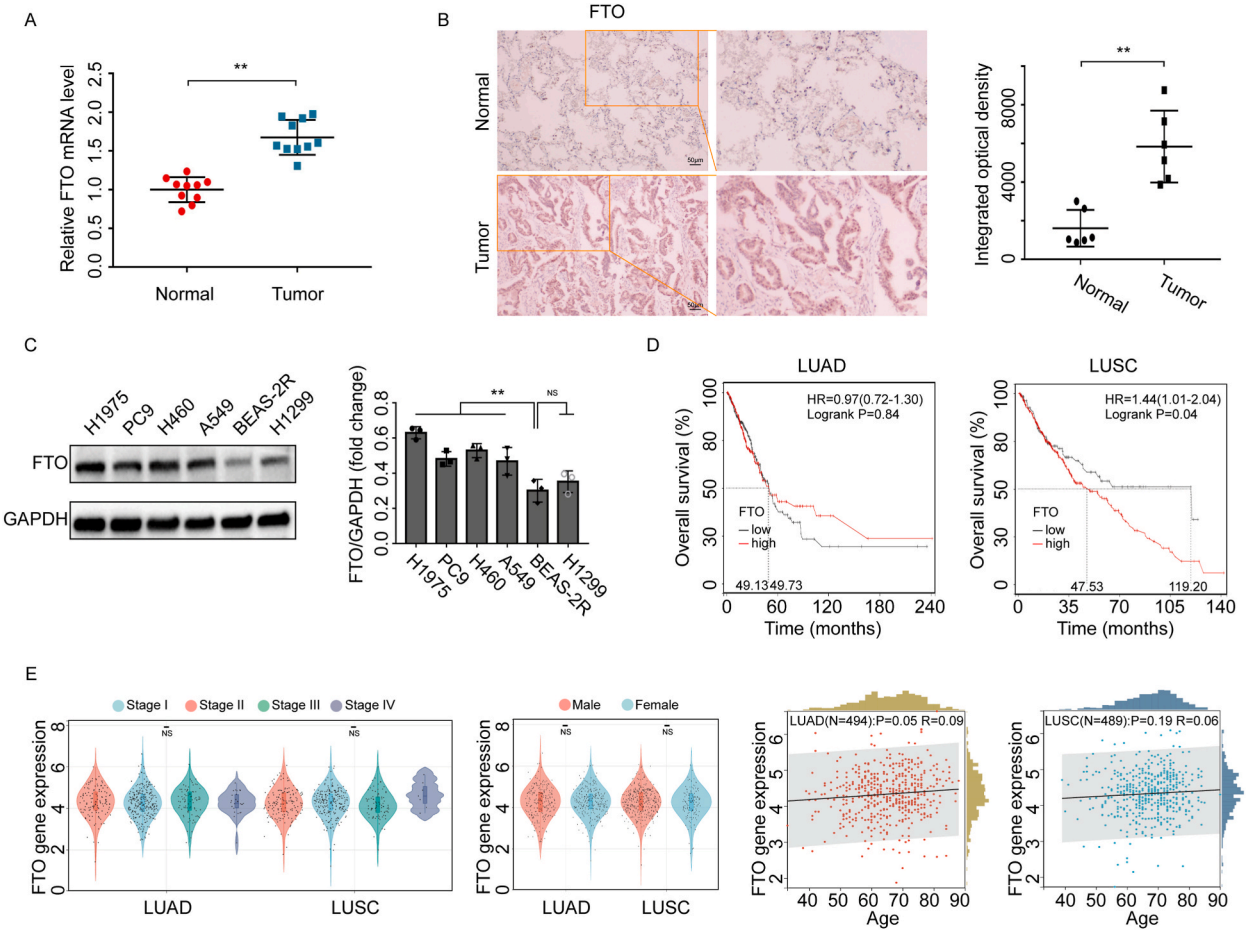

Fig. 1. Increased *FTO* expression impairs the prognosis of NSCLC patients. (A) Relative mRNA levels of *FTO* in 10 pairs of human NSCLC tissues and their adjacent normal tissues were detected by RT–PCR (n = 10, paired-samples T test). (B) Representative immunohistochemical staining of FTO in six pairs of human NSCLC tissues and their adjacent normal tissues (n = 6, paired-samples T test). Scale bar: 50 μm. (C) FTO expression in H1975, PC9, H460, A549, H1299, and BEAS-2R cells were measured using Western blotting (n = 3, one-way ANOVA). (D) Kaplan–Meier analysis displayed overall survival of LUAD (n = 494) and LUSC (n = 489) patients based on the UCSC Xena (Kaplan–Meier and log-rank test). (E) Correlation analysis of *SESN2* expression with clinical stage, gender, and age of LUAD and LUSC patients based on the UCSC Xena. Clinical stage (one-way ANOVA): LUAD (Stage I = 274, II = 122, III = 83, IV = 26), LUSC (Stage I = 242, II = 161, III = 84, IV = 7); Gender (paired-samples T test): LUAD (FEMALE = 276, MALE = 237), LUSC (FEMALE = 129, MALE = 369); Age (Pearson correlation analysis): LUAD (n = 494), LUSC (n = 489). Data are presented as means ± SD of three independent experiments. $^{**}P < 0.01$, NS stands for no significance. Uncropped versions of Fig. 1C were added to Supplemental Material.

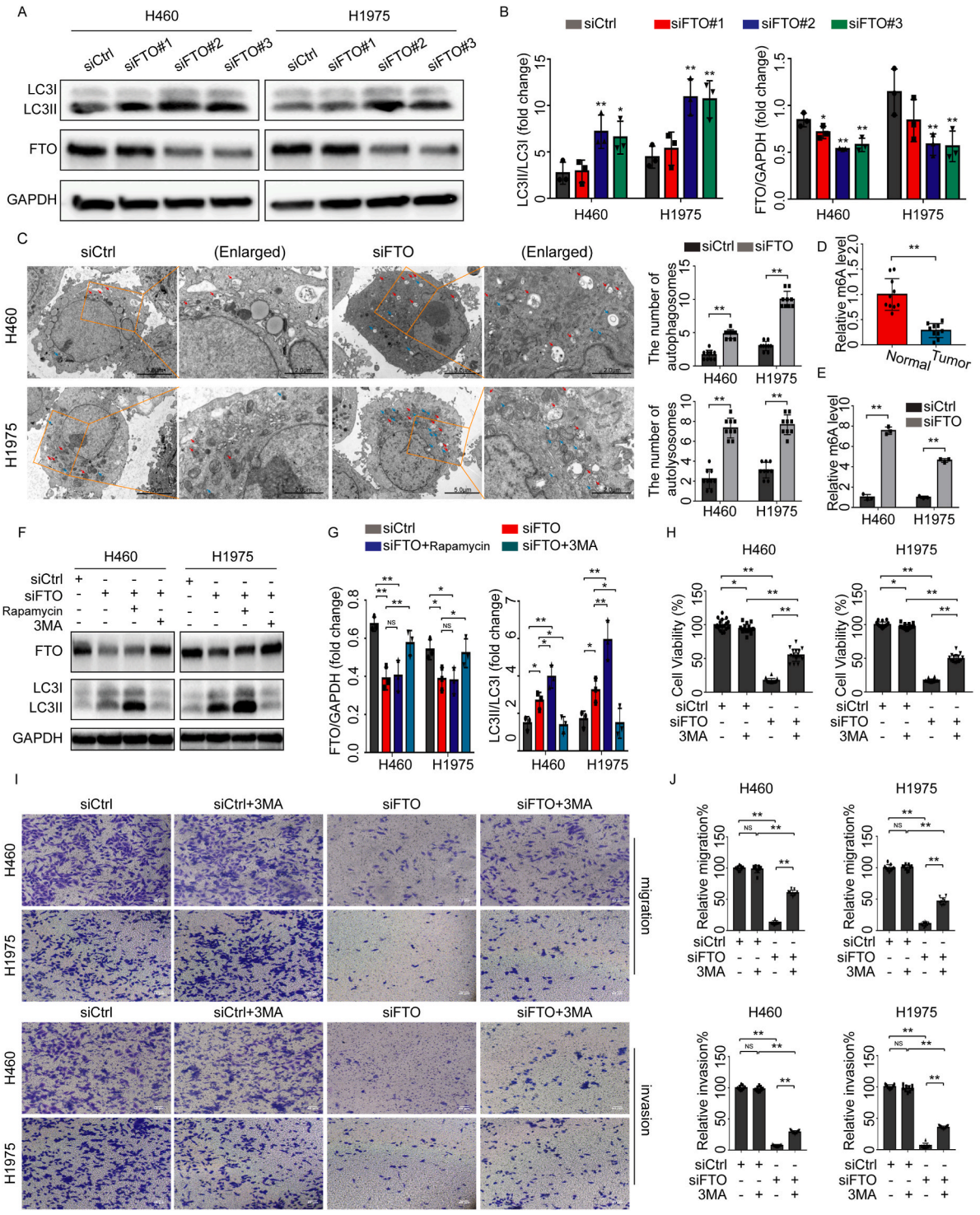

Fig. 2. Downregulation of *FTO* blocks the growth, invasion and migration of NSCLC cells via induction of autophagy. (A–B) Three distinct siRNAs (siFTO#1, siFTO#2, siFTO#3) were transfected into H460 and H1975 cells. The protein levels of LC3I, LC3II, and FTO were detected and quantified by Western blotting (n = 3, one-way ANOVA). (C) Transmission electron microscopy revealed autophagosomes and autolysosomes in *FTO*-knockdown H460 and H1975 cells (n = 3, paired-samples T test). Blue arrow, autophagosome; Red arrow, autolysosome. Scale bar (left): 5 μm; scale bar (right): 2 μm. (D) Relative m^6A levels were detected in 10 pairs of human NSCLC tissues and their adjacent normal tissues (n = 10, paired-samples T test). (E) Relative m^6A levels were detected in *FTO*-deficient H460 and H1975 cells (n = 3, paired-samples T test). (F–G) Western blotting was used to detect protein levels of FTO, LC3I, and LC3II in *FTO*-deficient H460 and H1975 cells treated with 100 nM rapamycin or 1 mM 3 MA for 24h (n = 3, one-way ANOVA). (H) Cell viabilities of *FTO*-deficient H460 and H1975 cells treated with or without 1 mM 3 MA for 48h were

detected by MTT assay (n = 6, one-way ANOVA). (I–J) Invasion and migration of *FTO*-deficient H460 and H1975 cells treated with or without 1 mM 3 MA for 48h were determined by a Transwell assay (n = 3, one-way ANOVA). Scale bar: 40 μm. Data are presented as means ± SD of three independent experiments. $^{*}P < 0.05$, $^{**}P < 0.01$, NS stands for no significance. Uncropped versions of Fig. 2A and F were added to Supplemental Material.

2.16. Tumor xenografts

Twenty female BALB/c-Nude mice (18–20 g each) were purchased from GemPharmatech (Chengdu, China) and housed in a specific-pathogen-free facility at the Experimental Animal Center of Southwest Medical University. The mice were randomly divided into shCtrl and shFTO groups, with five mice per group. After 5 days of adaptive feeding, 6×10^6 H460 cells were injected either subcutaneously (sc) or intravenously (iv) into the mice to establish tumor formation or lung metastasis models, respectively. Subsequently, tumor volume and body weight were measured every second day using a digital caliper [30]. General symptoms were observed and recorded daily. At the end of the experiment, the mice were sacrificed, and tumor tissues and lung metastases were isolated. After quantifying tumor weight and tumor metastases, some tumors were stained with hematoxylin & eosin for histopathological analysis, while the others were subjected to immunofluorescence and Western blotting to detect SESN2 protein levels. This study was reviewed and approved by the Animal Research Ethics Committee of Southwest Medical University (approval number: 20211124-039). Moreover, it complied with the ARRIVE guidelines and was conducted in accordance with the U.K. Animals (Scientific Procedures) Act, 1986 and its associated guidelines.

2.17. Bioinformatic analysis

We acquired expression data of key gene in lung adenocarcinoma (LUAD) and lung squamous cell carcinoma (LUSC) from standard pan-cancer dataset (The Cancer Genome Atlas, TARGET, Genotype–Tissue Expression [PANCAN, N = 19131, G = 60499]) hosted on the UCSC Xena portal (https://xenabrowser.net/). Samples with zero expression levels were eliminated, and the data underwent a $\log_2(x + 0.001)$ transformation. Finally, differential gene expression, prognostic, and multivariable analyses based on clinical stage, gender, and age were performed using R (version 3.6.4).

2.18. Statistical analysis

Statistical analysis was conducted using SPSS version 13.0 (Chicago, IL, USA). Data related to cell lines were repeated at least three times and were expressed as the mean ± standard deviation (SD). One-way analysis of variance (ANOVA) followed by least significant difference (LSD) post hoc tests were applied to assess differences between multiple groups, assuming equal variances among the groups. Otherwise, Dunnett's T3 test was used for multi-group comparisons. Paired-samples T test was performed to compare differences between two groups. Kaplan-Meier method and log-rank test were used for survival analysis. $P < 0.05$ was considered statistically significant.

3. Results

3.1. Increased FTO expression impairs the prognosis of NSCLC patients

We first measured FTO expression in human NSCLC tissues and adjacent normal tissues. The expression of FTO was significantly higher in NSCLC tissues compared with their adjacent normal tissues at both the mRNA and protein levels (Fig. 1A and B). *In vitro,* compared with the normal human lung bronchial epithelial cell line BEAS-2R, FTO protein levels were dramatically elevated in multiple lung cancer cell lines, including H1975, H460, PC9, A549 (Fig. 1C). Next, we retrieved the pan-cancer dataset [35] from UCSC Xena and extracted relevant *FTO* gene data in LUSC and LUAD samples. The overall survival rate of LUSC patients with high *FTO* expression was remarkably lower than that of patients with low *FTO* expression, whereas the overall survival rate of LUAD patients was unaffected by *FTO* expression levels (Fig. 1D). In addition, *FTO* expression was not associated with distinct clinical stage, age, and gender (Fig. 1E). Overall, these results suggest that increased *FTO* expression may be an independent prognostic factor affecting the overall survival of LUSC patients.

3.2. Downregulation of FTO suppresses the growth, invasion and migration of NSCLC cells by inducing autophagy

To explore the relationship between *FTO* expression and autophagy in NSCLC cells, three distinct siRNAs (#1, #2, #3) were used to silence FTO expression in H460 and H1975 cells. Western blotting showed that FTO expression was markedly reduced in both cell lines after transfection with siFTO#2 and siFTO#3 (Fig. 2A and B). Meanwhile, downregulation of *FTO* significantly increased the ratio of microtubule-associated protein light chain 3-II (LC3II) to LC3I compared with the control group, indicating autophagosome formation (Fig. 2A and B). We assessed autophagic flux by transfecting cells with the RFP-GFP-LC3 vector. Autophagosomes fuse with lysosomes to form autolysosomes, which is accompanied by quenching of the fluorescence of green fluorescent protein. Thus, yellow dots indicate autophagosomes and red dots indicate autolysosomes [36]. The number and fluorescence intensity of red dots significantly increased in *FTO*-knockdown cells (Figs. S1A–B). This was corroborated through transmission electron microscopy (Fig. 2C), verifying that *FTO*

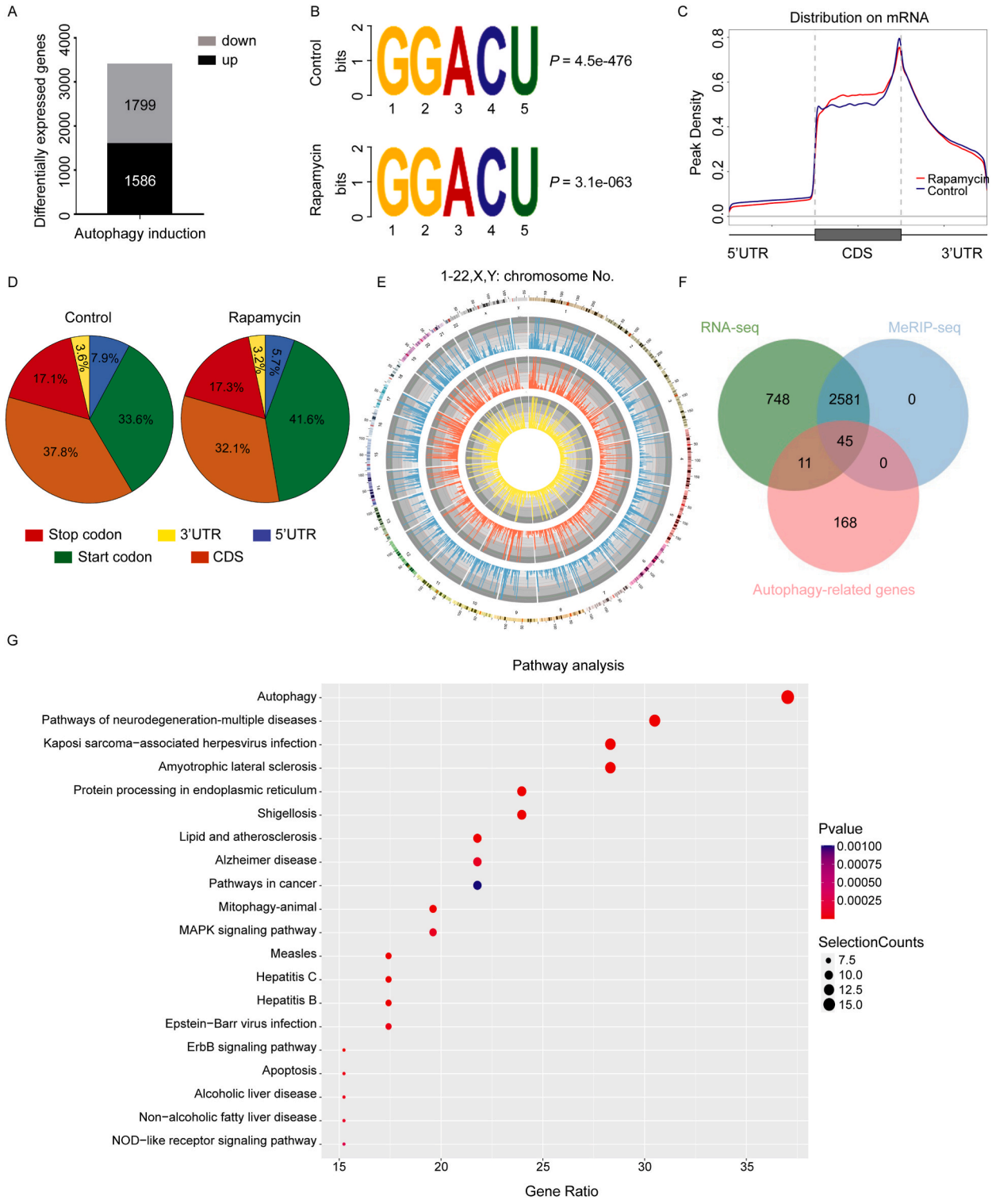

Fig. 3. Autophagy-mediated alterations to m^{6}A-modified transcripts in NSCLC cells. (A) DEGs with fold-change greater than 2.0 in H460 cells treated with or without 100 nM rapamycin for 24h. (B) The m^{6}A motif in autophagy-activated H460 cells was identified by MEME motif analysis using MeRIP-seq data. (C) Metagene profiles of m^{6}A enrichment in the mRNA transcriptome of H460 cells with and without rapamycin treatment. (D) Distribution pie charts of m^{6}A sites across distinct gene regions in control and rapamycin-treated H460 cells. (E) Circos plot of m^{6}A peak distribution in the transcriptome of rapamycin-treated H460 cells. (F) Venn diagram showing the overlap of differential genes identified by MeRIP-seq and RNA-seq with autophagy-related genes. (G) KEGG enrichment analysis of 45 overlapping DMGs.

downregulation activated autophagy. We selected siFTO#2 for our subsequent experiments.

We explored FTO-regulated m^{6}A modifications. It was found that m^{6}A levels were significantly lower in human NSCLC tissues than in their adjacent normal tissues (Fig. 2D), which was consistent with the findings of Liu et al. [16]. Increased m^{6}A levels were also observed in *FTO*-deficient NSCLC cells (Fig. 2E).

Compared with the control group, downregulation of *FTO* or co-treatment with rapamycin attenuated FTO protein expression and elevated the LC3II/LC3I ratio in both NSCLC cell lines. 3 MA has been found to block autophagosome formation by inhibiting class III phosphoinositide-3-kinase, which in turn suppresses the early autophagic flux [37]. Conversely, 3 MA treatment markedly restored FTO levels and blocked the conversion of LC3I to LC3II in *FTO*-deficient cells (Fig. 2F and G). Further, we investigated the role of FTO-regulated autophagy in the progression of NSCLC. Transwell and cell viability assays showed that *FTO*-deficient cells exhibited lower growth, invasion, and migration, whereas treatment with 3 MA partially rescued these cell behaviors (Fig. 2H–J). Collectively, these data suggest that *FTO* downregulation significantly inhibits the growth, invasion and migration of H460 and H1975 cells by inducing autophagy.

3.3. *SESN2 is involved in m^{6}A regulation during autophagy in NSCLC cells*

To investigate changes in the extent of m^{6}A modifications of specific genes in autophagic cells, we performed MeRIP-seq and RNA-seq analyses on autophagy-activated H460 cells. RNA-seq revealed that 1586 differentially expressed genes (DEGs) were significantly upregulated and 1799 DEGs were downregulated (Fig. 3A, Table S1 and Table S2). MeRIP-seq uncovered that GGACU co-recognition

Table 3
Forty-five common genes involved in autophagy and m^{6}A regulation.

Gene name	log_2FC(m6A peak)	logFC(gene expression)
AMBRA1	7.098032083	1.747773961
FOS	5.833383792	6.57993611
PELP1	5.760220946	−1.638314173
SAR1A	4.972519264	1.367723112
PPP1R15A	4.87786227	5.001121979
ERN1	4.411999789	2.097006478
MAP1LC3B	4.311586151	3.585395633
SESN2	4.040089006	3.920495411
FOXO3	3.938026704	2.481707822
MAPK8IP1	3.871341698	−7.121752368
DDIT3	3.719042762	3.496168984
DNAJB1	3.249011839	1.40385499
EIF2AK3	3.036587634	2.310463641
ATG4A	2.892795766	1.599613584
TBK1	2.738693816	1.088725462
ZFYVE1	2.702489163	2.765184214
NPC1	2.626431677	1.286097975
CHMP2B	2.537679588	2.808317883
GNAI3	2.529219949	1.904620778
MAPK8	2.509273569	1.560107079
MAPK9	2.35414272	−1.549282218
SIRT1	2.317912455	2.959692426
CDKN1A	2.105384955	1.85800979
WIPI2	2.055482557	1.086882345
RAB33B	2.046501273	2.499042705
DNAJB9	2.029219207	2.423552803
RELA	1.969447669	−2.672457
HSPA5	1.796329398	1.486268454
ATG3	1.734822178	2.35745156
ATG16L1	1.696174959	1.205704107
ATG14	1.483248078	2.119475874
BAG3	1.45568447	2.123567552
ATG4C	−1.432126392	−4.764881213
CAMKK2	−1.726093689	−2.787492977
HSPA8	−1.736989012	−1.264660016
MYC	−1.825751857	−1.328918344
NRG2	−1.856382205	−6.91385535
HIF1A	−1.902214108	−1.127686825
NRG1	−1.986515155	−3.146586505
CASP4	−2.197516387	−2.864763838
EGFR	−2.431034602	−3.295923621
HDAC6	−2.548305789	−3.457567587
RB1	−2.707155146	−1.829657626
EEF2K	−2.898397792	−4.01079435
EIF2AK2	−3.682452638	−1.61227484

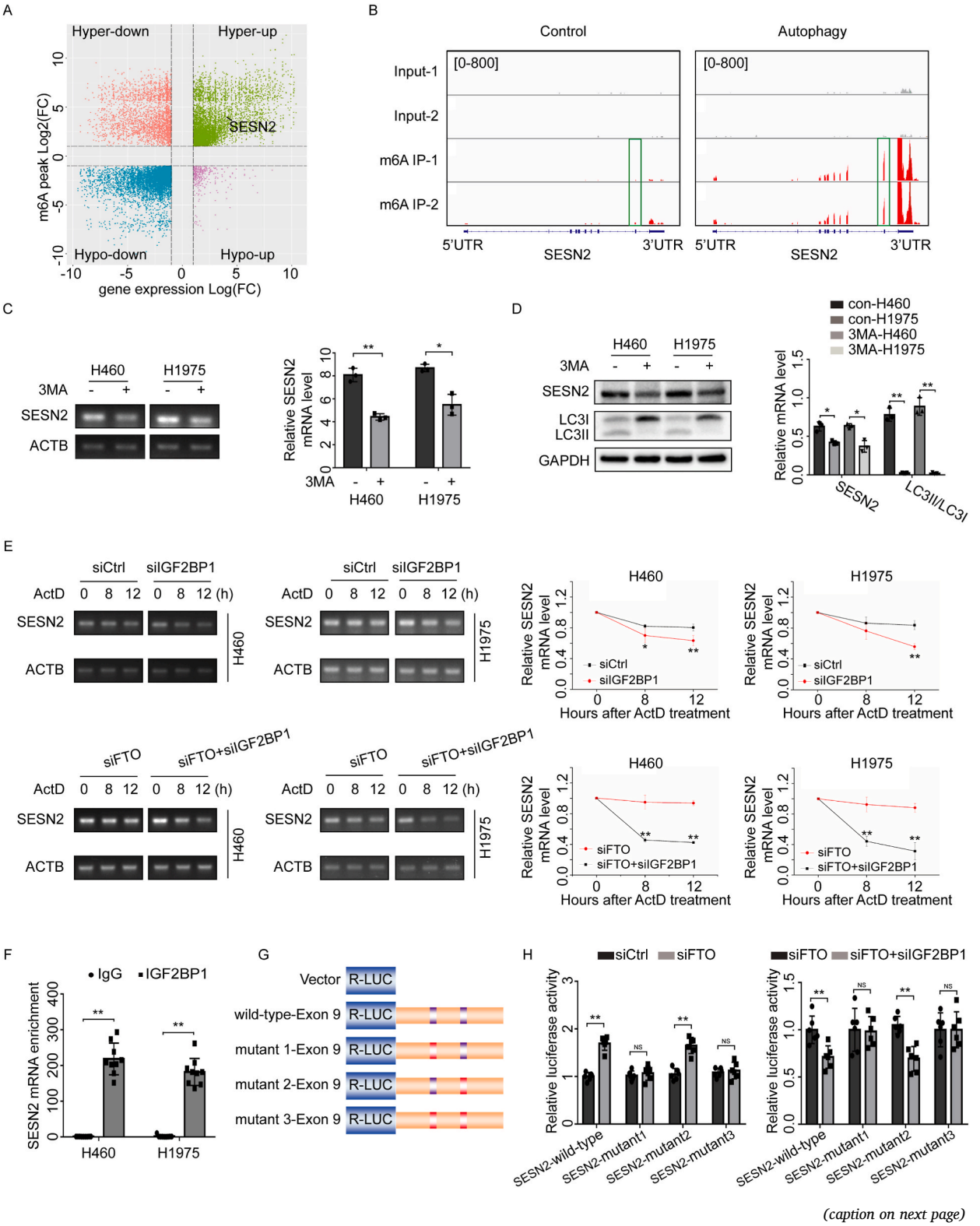

(caption on next page)

Fig. 4. SESN2 is involved in m^{6}A regulation during autophagy in NSCLC cells. (A) Localization of *SESN2* in quartile quadrant plots of peak distributions. (B) Integrative genomics viewer plots displaying multiple m^{6}A peaks in *SESN2* mRNA. (C) Relative mRNA levels of *SESN2* in H460 and H1975 cells treated with 1 mM 3 MA for 24h (n = 3, paired-samples T test). (D) Western blotting revealed protein levels of SESN2, LC3I, and LC3II in H460 and H1975 cells treated with 1 mM 3 MA for 24h (n = 3, paired-samples T test). (E) RNA stability assay exhibited degradation of *SESN2* mRNA in *FTO*-deficient cells with or without *IGF2BP1* knockdown. Cells were treated with 5 μg/mL ActD for 0, 8, 12h and then analyzed by RT–PCR (n = 3, paired-samples T test). (F) Enrichment of IGF2BP1 with *SESN2* mRNA was analyzed by RIP–qPCR using an IGF2BP1-specific antibody in *FTO*-deficient H460 and H1975 cells (n = 3, paired-samples T test). (G) Schematic diagram showing luciferase reporters and other reporters, such as wild-type and mutant 1–3 *SESN2* exon 9 (A in GGAC replaced by T). (H) Relative luciferase activities of SESN2-wild-type/SESN2-mutant reporter vectors in control, *FTO*-knockdown, and *FTO* and *IGF2BP1* double-knockdown H460 cells (n = 6, paired-samples T test). $^*P < 0.05$, $^{**}P < 0.01$. Data are presented as means ± SD of three independent experiments. $^*P < 0.05$, $^{**}P < 0.01$, NS stands for no significance. Uncropped versions of Fig. 4C–E were added to Supplemental Material.

motifs were enriched in autophagic cells (Fig. 3B), suggesting significant m^{6}A-modifying activity during autophagy, which is aligned with previously published results [38,39]. These m^{6}A peaks were particularly enriched in the 3′UTR and the coding sequence (CDS) region (Fig. 3C and D). Fig. 3E displays a Circos plot illustrating the distribution of m^{6}A modifications in the transcriptome of autophagic H460 cells. We compared the differentially modified genes between the RNA-seq and MeRIP-seq datasets and overlaid them with 234 known autophagy-related genes to identify 45 common genes, which can be potential candidates regulating m^{6}A modifications during autophagy (Fig. 3F and Table 3). Gene Ontology (GO) & Kyoto Encyclopedia of Genes and Genomes (KEGG) enrichment analyses showed that these candidate genes were mainly associated with autophagy, gene transcription regulation, apoptosis, stress response, etc. (Fig. 3G and Figs. S2A–C).

Among these 45 candidate genes involved in m^{6}A regulation, members of our research group have explored mechanisms of the first 8 genes hypermethylated by m^{6}A (*AMBRA1*, *FOS*, *PELP1*, *SAR1A*, *PPP1R15A*, *ERN1*, *MAP1LC3B*, *SESN2*) in the progression of NSCLC cells. *SESN2* encodes a stress response protein that plays a crucial role in regulating cell growth and apoptosis, and may participate in cellular responses to various stressors, including autophagy, oxidative stress, endoplasmic reticulum stress, DNA damage, and inflammation [40,41]. In this study, *SESN2* was also hypermethylated during autophagy (Fig. 4A, Table 3). MeRIP-seq data demonstrated that m^{6}A modifications increased in the 3′ UTR and CDS regions of *SESN2* mRNA during autophagy (Fig. 4B). Additionally, the m^{6}A peak of *SESN2* exon 9 (chr1:28,605,611–chr1:28,605,750) was highly enriched in autophagic H460 cells, with two 5′-GGAC-3′ sequences (Fig. 4B and Figs. S3A–B). However, SESN2 expression decreased at both the mRNA and protein levels after 3 MA treatment (Fig. 4C and D). We speculate that the m^{6}A modification of *SESN2* may regulate its stability during autophagy.

m^{6}A modifications are known to influence the stability and degradation of mRNAs, both of which are closely related to m^{6}A-binding proteins [42–44]. Insulin like growth factor 2 mRNA binding protein 1 (IGF2BP1) serves as a major m6A reader that specifically recognizes and stabilizes m^{6}A-modified mRNAs [34,45,46]. We explored whether IGF2BP1 could target m^{6}A sites on *SESN2* transcripts. Upon transcriptional blockade by ActD, *SESN2* was more efficiently degraded in *FTO* and *IGF2BP1* double-knockdown cells compared with *FTO*-knockdown cells (Fig. 4E). Loss of IGF2BP1 not only reduced *SESN2* stability but also promoted its degradation, which was already induced by *FTO* deletion (Fig. 4E). Further, RIP confirmed significant enrichment of *SESN2* using IGF2BP1 antibodies in *FTO*-deficient cells (Fig. 4F), suggesting that IGF2BP1 binds to *SESN2*.

We performed luciferase reporter gene assays and mutagenesis assays to explore the role of m^{6}A-modified *SESN2* in *FTO*- and *IGF2BP1*-mediated gene regulation. We engineered a luciferase reporter and other reporters, such as wild-type and mutant 1–3 *SESN2* exon 9 ("A" in GGAC replaced by "T"; Fig. 4G). *FTO* deletion resulted in increased luciferase activities in the wild-type and mutant 2 reporter genes, whereas the luciferase activities of mutant 1 and mutant 3 reporter genes were unaffected (Fig. 4H). Silencing of both *IGF2BP1* and *FTO* reduced the luciferase activities of wild-type and mutant 2 reporter genes, whereas the luciferase activities of mutant 1 and mutant 3 reporter genes were not significantly affected (Fig. 4H). Taken together, these results suggest that m^{6}A modification of *SESN2* in exon 9 is involved in regulating its mRNA stability.

3.4. Effect of FTO-regulated SESN2 expression on autophagic flux and malignant progression in NSCLC cells

To investigate the role of SESN2 in NSCLC progression, we transfected NSCLC cells with distinct concentrations of plasmids encoding SESN2. Overexpression of SESN2 significantly increased the LC3II/LC3I ratio (Fig. 5A and B), suggesting the activation of autophagic flux. Conversely, overexpression of FTO attenuated SESN2 expression and the LC3II/LC3I ratio (Fig. 5B). Overexpression of the H231A mutant of FTO [23,47], however, did not reduce SESN2 expression and failed to inhibit the turnover of LC3I to LC3II (Fig. 5B). The total extent of m^{6}A modifications was remarkably reduced in FTO-overexpressing NSCLC cells, whereas overexpression of the FTO mutant failed to reduce total m^{6}A levels (Fig. 5C). These results suggest that FTO-regulated SESN2 expression affects autophagic flux through the demethylase activity of FTO.

Moreover, upregulation of *SESN2* led to an increase in the number of autophagososomes and/or autolysosomes, but *FTO*-overexpression or treatment with the autophagy inhibitor 3 MA markedly negated this phenomenon (Fig. 5D and Figs. S4A–B). Importantly, *SESN2* upregulation inhibited the proliferation, invasion and migration of H460 and H1975 cells, while 3 MA treatment or *FTO* overexpression partially reversed these effects (Fig. 5E and F).

Collectively, these results suggest that FTO inhibits autophagic flux by down-regulating *SESN2*, which promotes the growth, invasion and migration of NSCLC cells.

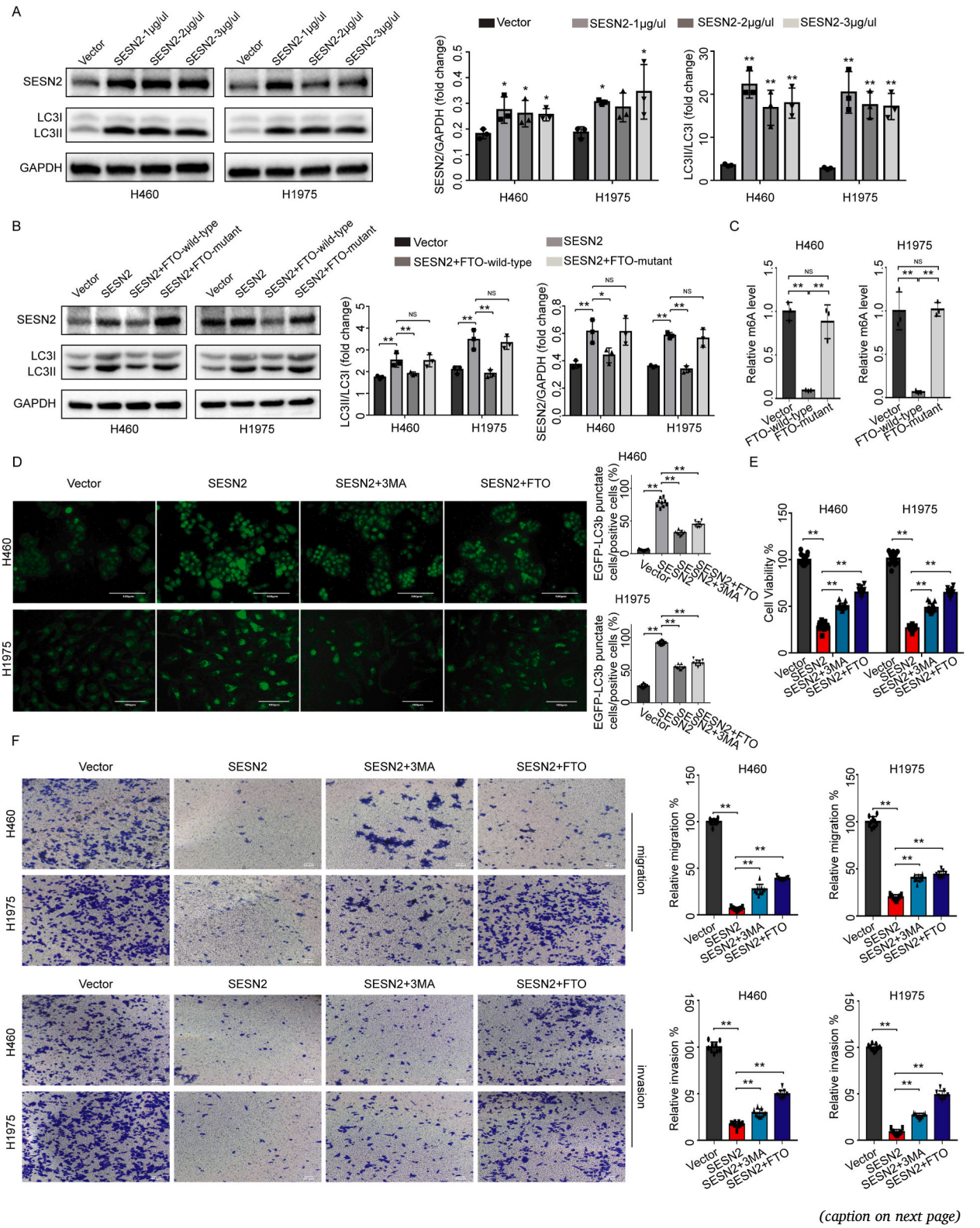

(caption on next page)

Fig. 5. Effect of FTO-regulated *SESN2* expression on autophagic flux and malignant progression in NSCLC cells. (A) Western blotting showed protein levels of SESN2, LC3I and LC3II in H460 and H1975 cells transfected with *SESN2* overexpression plasmid for 24h (n = 3, one-way ANOVA). (B) Western blotting to detect SESN2, LC3I, and LC3II expression in H460 and H1975 cells overexpressing *SESN2* along with wild-type or mutant FTO (n = 3, one-way ANOVA). (C) Relative m^6A levels were detected in FTO-wild-type and FTO-mutant H460 and H1975 cells (n = 3, one-way ANOVA). (D) EGFP-LC3b plasmid was transfected into H460 and H1975 cells to construct stably transfected cell lines. Immunofluorescence demonstrated the fluorescence intensity of autophagosomes in control and *SESN2*-overexpressing cells with *FTO* overexpression or 3 MA treatment for 24h (n = 3, one-way ANOVA). Scale bar: 100 μm. (E) Cell viabilities of H460 and H1975 cells overexpressing *SESN2* along with *FTO* overexpression or 3 MA treatment for 48h were detected by MTT assay (n = 6, one-way ANOVA). (F) Invasion and migration of H460 and H1975 cells overexpressing *SESN2* along with *FTO* overexpression or 3 MA treatment for 48h were determined by a Transwell assay (n = 3, one-way ANOVA). Scale bar: 40 μm. Data are presented as means ± SD of three independent experiments. $^*P < 0.05$, $^{**}P < 0.01$, NS stands for no significance. Uncropped versions of Fig. 5A–B were added to Supplemental Material.

3.5. FTO-regulated SESN2 expression affects the AMPK-mTOR signaling pathway

The AMPK-mTOR signaling pathway plays a crucial role in the activation of autophagy [48]. It has been shown that SESN2 impedes the progression of tumor cells by increasing the phosphorylation of AMPKα and negatively regulating mTOR [49]. Therefore, is the effect of FTO-regulated SESN2 expression on autophagy related to AMPK-mTOR signaling pathway? We found that the relative fluorescence intensity (RFI) of p62 protein was significantly reduced in *SESN2*-overexpressing H460 and H1975 cells; conversely, overexpression of *FTO* increased the RFI of p62 protein to a certain extent (Fig. 6A), further suggesting that FTO could block SESN2-mediated autophagy activation. Furthermore, *SESN2* upregulation resulted in an increase in phospho-AMPKα (Thr172) and a

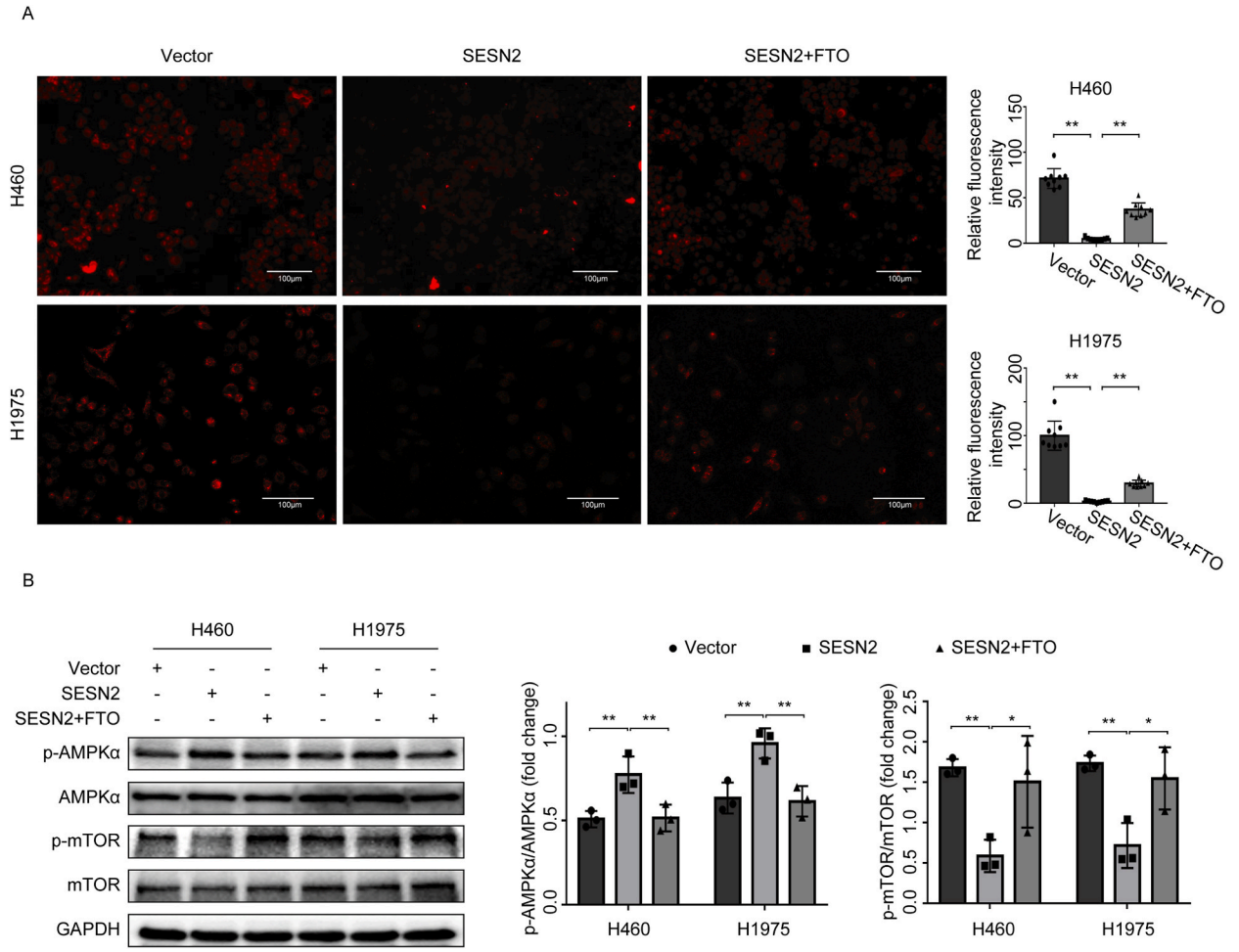

Fig. 6. FTO-regulated SESN2 expression affects the AMPK-mTOR signaling pathway. (A) Representative immunofluorescence images of H460 and H1975 cells overexpressing *SESN2* along with *FTO* overexpression. Immunofluorescence demonstrated the fluorescence intensity of p62 in these cells (n = 3, one-way ANOVA). Scale bar: 100 μm. (B) Western blotting to detect *p*-AMPKα, AMPKα, *p*-mTOR, mTOR expression in H460 and H1975 cells overexpressing *SESN2* along with *FTO* overexpression (n = 3, one-way ANOVA). Data are presented as means ± SD of three independent experiments. $^*P < 0.05$, $^{**}P < 0.01$. Uncropped versions of Fig. 6B were added to Supplemental Material.

decrease in phospho-mTOR (Ser2448), indicating activation of AMPKα and negative regulation of mTOR by *SESN2* overexpression (Fig. 6B). However, overexpression of *FTO* markedly inhibited the activation of AMPKα and promoted positive regulation of mTOR (Fig. 6B). In conclusion, these results suggest that the mechanism by which FTO impedes SESN2-mediated autophagy activation is

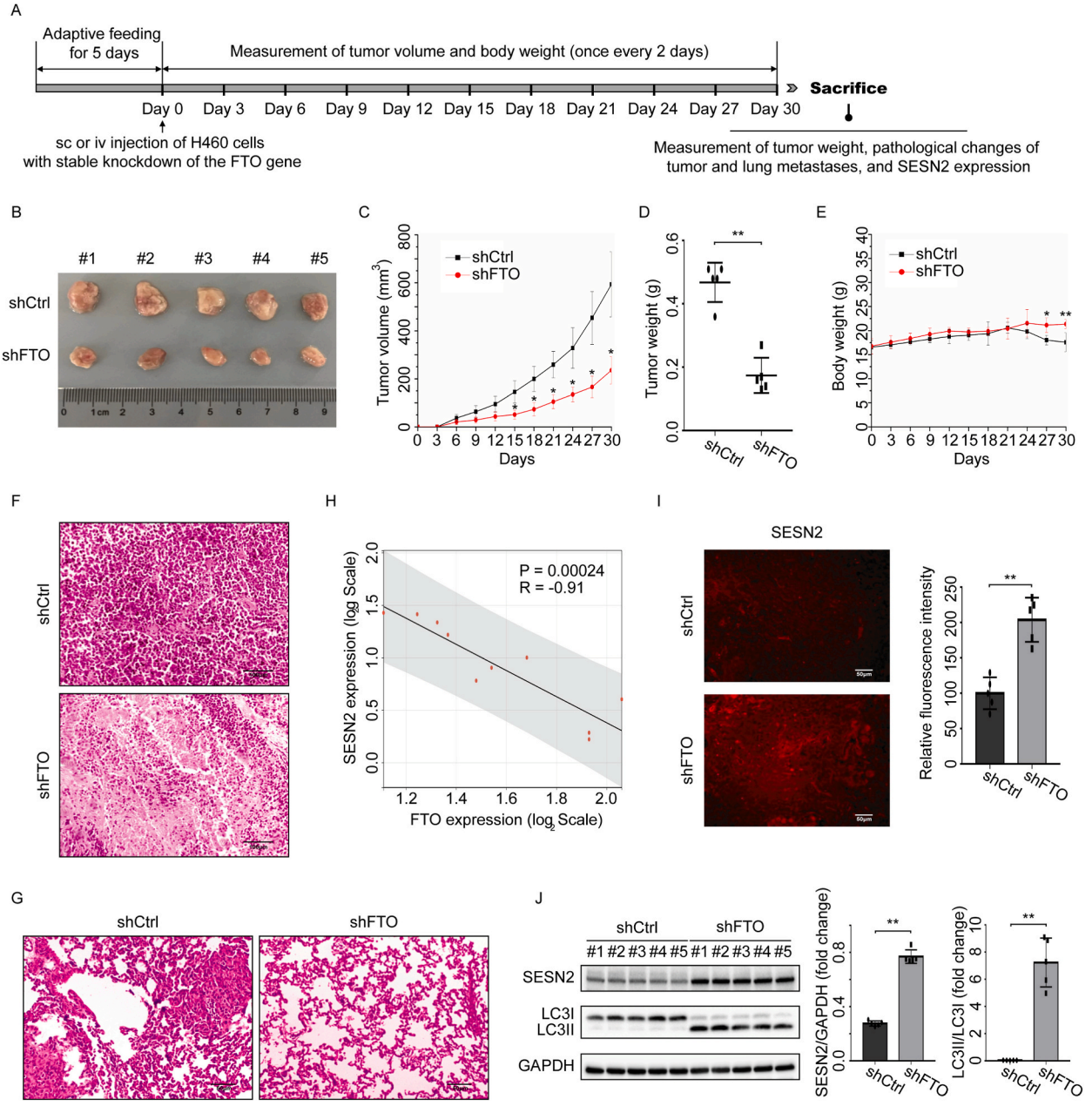

Fig. 7. *In vivo* validation of the tumorigenic effect of FTO in NSCLC and its correlation with *SESN2* expression. (A) Experimental design. (B) The dissected tumors in control and *FTO*-knockdown groups (n = 5). (C) Tumor volumes in control and *FTO*-knockdown groups (n = 5, paired-samples T test). (D) Tumor weights in control and *FTO*-knockdown groups (n = 5, paired-samples T test). (E) Body weight of mice in control and *FTO*-knockdown groups (n = 5, paired-samples T test). (F) Representative HE staining images of transplanted NSCLC tumors from control and *FTO*-knockdown groups. HE staining showed the pathologic changes in NSCLC tumors from the two groups. Scale bar: 100 μm. (G) Representative HE staining images of lung metastases from control and *FTO*-knockdown groups. HE staining displayed the pathologic changes in lung metastases from the two groups. Scale bar: 50 μm (H) Pearson correlation analysis of *FTO* and *SESN2* mRNA expression in tumor tissues from 10 NSCLC patients (n = 10). (I) Representative immunofluorescence images of transplanted NSCLC tumors from control and *FTO*-knockdown groups. Immunofluorescence demonstrated the fluorescence intensity and localization of *SESN2* in tumor tissues from the two groups (n = 5, paired-samples T test). Scale bar: 50 μm. (J) Western blotting to detect SESN2, LC3I and LC3II expression in the transplanted NSCLC tumors from the control and *FTO*-knockdown groups (n = 5, paired-samples T test). $^{*}P < 0.05$, $^{**}P < 0.01$. Uncropped versions of Fig. 7J were added to Supplemental Material.

associated with the AMPK-mTOR signaling pathway.

3.6. *In vivo validation of the tumorigenic effect of FTO in NSCLC and its correlation with SESN2 expression*

To investigate the *in vivo* oncogenic role of FTO in NSCLC, stably transfected H460 cells harboring *FTO* knockdown were injected sc or iv into immune-deficient nude mice to construct tumor-bearing or lung metastasis mouse models (Fig. 7A). Compared with the control group, loss of *FTO* significantly reduced tumor volume and tumor weight (Fig. 7B–D). From day 27 onwards, body weight of mice in the control group was markedly decreased compared with those in the *FTO*-deficient group (Fig. 7E). Tumor cells in the control group exhibited dense growth and deeply stained nuclei, whereas downregulation of *FTO* resulted in the death of a large number of tumor cells and nuclear consolidation, as evidenced by hematoxylin and eosin (HE) staining (Fig. 7F). Besides, *FTO* knockdown notably suppressed tumor metastasis (Fig. 7G).

FTO was negatively correlated with *SESN2* expression in tumor tissues from NSCLC patients, as evidenced by qPCR (Fig. 7H). In xenograft mouse models, *FTO* knockdown led to a 94.32% increase in the mean fluorescence intensity of *SESN2* relative the control group (Fig. 7I). Lung metastases from the *FTO*-deficient group exhibited significantly elevated SESN2 protein levels and LC3II/LC3I ratio (Fig. 7J). Altogether, these results confirm that FTO contributes to autophagy inhibition, growth and metastasis of NSCLC and is negatively correlated with *SESN2* expression in NSCLC.

4. Discussion

Lung cancer remains one of the most malignant cancers with the highest mortality rate worldwide. Therefore, elucidating the molecular mechanisms of tumorigenesis and progression is critical for developing rational interventions. In this study, we found that the m^{6}A demethylase FTO was significantly upregulated in human NSCLC, and downregulation of FTO obstructed the growth,

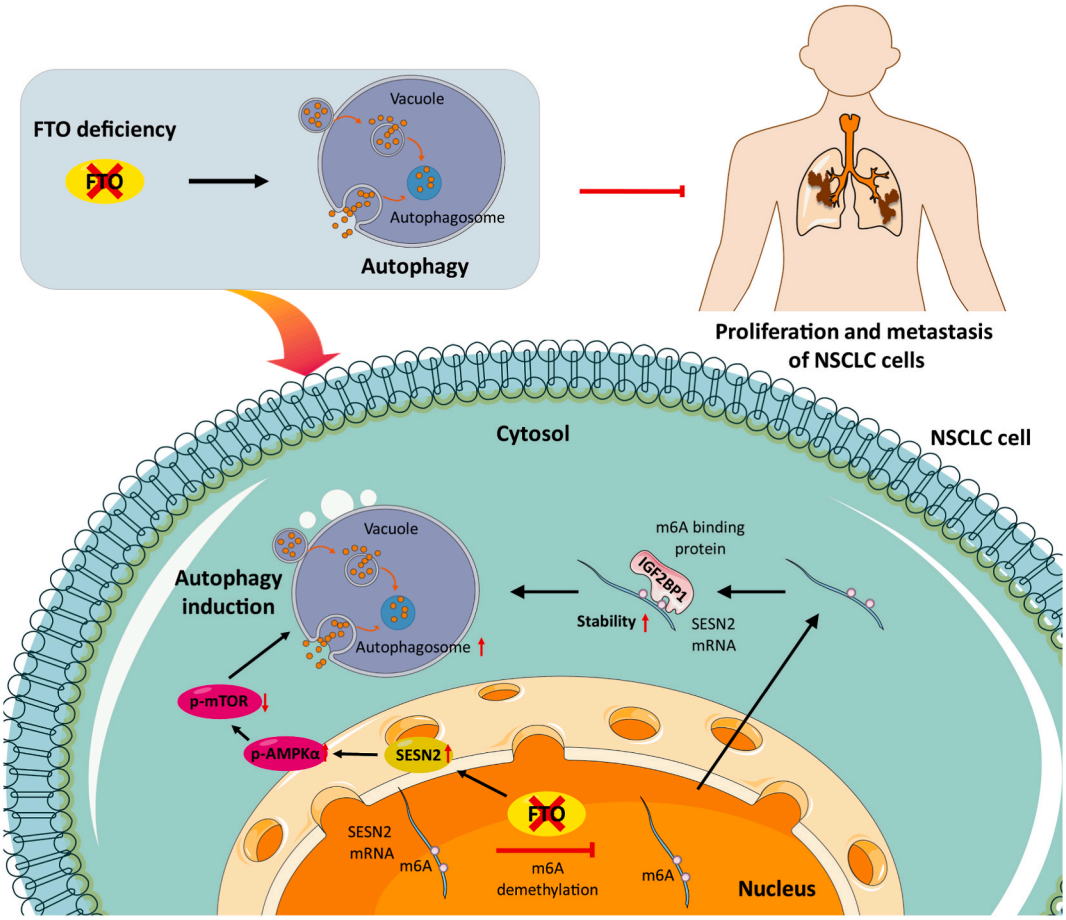

Fig. 8. Schematic diagram of the proposed mechanism by which *FTO* deletion-mediated autophagy inhibits the progression of NSCLC. FTO deficiency promoted the interaction between IGF2BP1 and *SESN2* mRNA, which enhanced *SESN2* mRNA stability and its protein expression, thereby promoting autophagy and mitigating the malignant progression of NSCLC. Besides, loss of *FTO* upregulated *SESN2* expression, which in turn induced autophagy through increased phosphorylation of AMPKα and negative regulation of mTOR.

invasion, and migration of NSCLC cells by inducing autophagy. Experiments on mouse xenograft models showed that loss of FTO promotes autophagy activation and suppresses tumor growth and lung metastasis. Importantly, we found that SESN2 was involved in regulating m^6A modifications during autophagy in NSCLC cells. *FTO* deficiency promoted the interaction between IGF2BP1 and *SESN2* mRNA, which enhanced *SESN2* mRNA stability and its protein expression, thereby promoting autophagy and mitigating the malignant progression of NSCLC (Fig. 8).

As an evolutionarily conserved mechanism of stress response, the role of autophagy in tumors is complex [50,51]. On the one hand, autophagy can degrade damaged organelles and defective proteins into nutrients for cellular metabolism, thus alleviating DNA damage, oxidative stress, inflammation, etc. and ultimately maintaining homeostasis and preventing the formation of malignant tumors. On the other hand, autophagy provides metabolites to tumor cells to promote their survival and metastasis once the tumor is formed. Increasing evidence suggests that autophagy impedes tumor progression and metastasis [23,24,52]. Autophagy promotes radiotherapy-induced cervical cancer cell death [53]. Autophagic cell death induced by some small molecule compounds blocks tumorigenesis and overcomes multidrug resistance [22,54–56]. Cadmium-induced malignant progression of breast cancer is associated with inhibition of autophagy mediated by acyl-coenzyme A synthetase short chain family member 2/autophagy-related gene 5 [57]. Hence, clarifying the key targets of autophagy holds great significance in improving the diagnosis and treatment of patients with specific cancers.

The m^6A modification of mRNA has been increasingly investigated in the context of cancer. Being the most prevalent mRNA modification in eukaryotes, m^6A regulates autophagy and plays a major role in diverse tumors. The demethylase FTO regulates m^6A modifications and exerts a pro-tumorigenic effect [58–61]. However, the role of FTO in regulating autophagy in tumor cells is controversial. *FTO* overexpression promoted the survival and reduced the apoptosis of ovarian cancer cells by activating autophagy [62]. *FTO* deletion hindered autophagy and enhanced chemotherapy efficacy in gastric cancer cells [63,64]. FTO-mediated autophagy inhibition promoted the growth and metastasis of clear cell renal cell carcinoma [24]. Deletion of *FTO* increased autophagy flux, which inhibited the malignant progression of oral squamous cell carcinoma [23]. Aligned with these studies, the present study showed that FTO was significantly upregulated in NSCLC, and its downregulation impeded the growth, invasion and migration of NSCLC cells by activating autophagic flux. Meanwhile, *FTO* deficiency induced autophagy and reduced the growth and metastasis of NSCLC cells in mouse xenograft models. Moreover, increased *FTO* expression may be an independent prognostic factor affecting overall survival of LUSC patients. These results verify that FTO can promote the malignant progression of NSCLC by inhibiting autophagic flux. However, in-depth mechanistic studies are still necessary.

MeRIP-seq and RNA-seq were performed on autophagy-activated NSCLC cells to investigate alterations in m^6A modifications of specific genes. We found SESN2 to be involved in regulating m^6A modifications during autophagy in NSCLC cells. SESN2 functions as a stress response protein that plays a critical role in regulating cell growth and apoptosis [65–67]. It is also implicated in cellular responses to stress processes, including autophagy, oxidative stress, endoplasmic reticulum stress, and DNA damage [41]. The results of this study indicated that the levels of m^6A modifications of *SESN2* increased during autophagy, mainly being enriched in the 3′ UTR and CDS regions. *SESN2* was hypermethylated during autophagy. These results suggest that *SESN2* is a target involved in regulating m^6A modifications during autophagy.

SESN2 blocks lung cancer progression by targeting the Akt–mammalian target of rapamycin–p70 S6 kinase signaling pathway [66]. Transcriptional activation of *SESN2* by isohapontigenin induces autophagy and impedes bladder cancer progression through the mitogen-activated protein kinase 8/Jun N-terminal kinase 1/Jun pathway [68]. The results of this study demonstrated that SESN2 contributes to autophagy activation and suppresses the growth, invasion and migration of NSCLC cells. The expressions of *FTO* and *SESN2* were found to be negatively correlated. Overexpression of *FTO* reduced *SESN2* levels and its m^6A content, thus inhibiting autophagic flux. Moreover, overexpression of demethylase-inactivated FTO mutants failed to reverse these changes, indicating that FTO-regulated SESN2 expression affected autophagy through the demethylase activity of FTO. The mechanism by which FTO impedes SESN2-mediated autophagy activation is associated with the AMPK-mTOR signaling pathway. Further, we revealed that FTO inhibits autophagic flux by downregulating *SESN2*, thereby promoting the growth, invasion, and migration of NSCLC cells.

m^6A modification of mRNA can alter its stability and degradation, both of which are closely related to m^6A-binding proteins [42–44]. IGF2BP1 functions as an important m^6A reader that specifically recognizes m^6A moieties on mRNA to prevent its degradation [42,43]. The present findings indicated that *FTO* deficiency promotes the IGF2BP1–*SESN2* interaction, which enhances the mRNA stability of *SESN2* and increases its protein expression. Specifically, m^6A modifications in exon 9 of *SESN2* were found to be involved in regulating the mRNA stability of *SESN2*.

Although we detected LC3B levels by Western blotting and quantified the number of autophagosomes and autolysosomes by transmission electron microscopy and the RFP-GFP-LC3 lentiviral vector, the methods utilized for autophagy assessment in this study still have some limitations. For example, it was not supplemented with other autophagy markers (Atg5/7, p62, Beclin1, etc.). In addition, the mechanism by which FTO inhibits autophagy will be explored in depth.

In summary, we have confirmed that FTO-mediated inhibition of autophagy promotes malignant progression of NSCLC by destabilizing *SESN2* mRNA. Besides, the mechanism by which FTO impedes SESN2-mediated autophagy activation is also associated with the AMPK-mTOR signaling pathway. These findings uncover an essential role of the FTO–autophagy–SESN2 axis in the malignant progression of NSCLC, suggesting that FTO is promising as a potential target and clinical prognostic marker for the prevention and treatment of NSCLC. Meanwhile, the strategy of autophagy induction and targeting FTO provides new insights into the diagnosis and treatment of NSCLC.

Funding statement

This study was financially supported by the Start-up Grant from Southwest Medical University (41/00040179), Applied Basic Research Program from Luzhou Science and Technology Bureau (2021-JXJ-55), Sichuan Natural Science Foundation Program from Sichuan Provincial Department of Science and Technology (2023NSFSC0741; 2023NSFSC0673), Scientific Research Program from Southwest Medical University (2021ZKQN108), Academic Promotion Programme of Shandong First Medical University (2019RC004), and the Special Fund for Taishan Scholars Project (tsqn201812149).

Data availability statement

Data included in article/supp. material/referenced in article:

CRediT authorship contribution statement

Kai Wang: Writing – review & editing, Writing – original draft, Project administration, Investigation, Funding acquisition, Conceptualization. **Zhiqiang Mei:** Writing – original draft, Validation. **Meiling Zheng:** Writing – review & editing. **Xiaoyan Liu:** Writing – review & editing. **Dabing Li:** Writing – review & editing, Writing – original draft, Funding acquisition. **Haiyong Wang:** Supervision, Project administration, Investigation, Funding acquisition, Conceptualization.

Declaration of competing interest

The authors declare that they have no known competing financial interests or personal relationships that could have appeared to influence the work reported in this paper.

Acknowledgements

The authors thank to all the participants, with special thanks to CLOUDSEQ (Shanghai, China) for their support in MeRIP-seq analysis. Besides, the authors also thank Bullet Edits Ltd. for their linguistic embellishments of this manuscript.

Appendix A. Supplementary data

Supplementary data to this article can be found online at https://doi.org/10.1016/j.heliyon.2024.e27571.

List of abbreviations

ActD	actinomycin D
ANOVA	analysis of variance
CDS	coding sequence
DEGs	differentially expressed genes
FTO	Fat mass and obesity-associated protein
GO	Gene Ontology
HE	hematoxylin and eosin
IGF2BP1	Insulin like growth factor 2 mRNA binding protein 1
iv	intravenously
KEGG	Kyoto Encyclopedia of Genes and Genomes
LC3	microtubule-associated protein light chain 3
LSD	least significant difference
LUAD	lung adenocarcinoma
LUSC:	lung squamous cell carcinoma
m6A	N6-methyladenosine;
MeRIP-seq	Methylated RNA immunoprecipitation sequencing
MTT	3-(4, 5-dimethylthiazol-2-yl)-2, 5-diphenyltetrazolium bromide;
NSCLC	Non-small cell lung cancer
qPCR	quantitative PCR
RFI	relative fluorescence intensity
RT–PCR	Reverse transcription-PCR
sc	subcutaneously
SD	standard deviation
SESN2	sestrin 2
shRNA	short hairpin RNA
siRNA	small interfering RNA

UTR untranslated region
3 MA 3-Methyladenine

References

[1] H. Sung, et al., Global cancer statistics 2020: GLOBOCAN estimates of incidence and mortality worldwide for 36 cancers in 185 countries, CA A Cancer J. Clin. 71 (3) (2021) 209–249.
[2] R. Ruiz-Cordero, W.P. Devine, Targeted therapy and checkpoint immunotherapy in lung cancer, Surgical pathology clinics 13 (1) (2020) 17–33.
[3] E.N. Imyanitov, A.G. Iyevleva, E.V. Levchenko, Molecular testing and targeted therapy for non-small cell lung cancer: current status and perspectives, Crit. Rev. Oncol.-Hematol. 157 (2021) 103194.
[4] E.B. Garon, et al., Five-year overall survival for patients with advanced non–small-cell lung cancer treated with pembrolizumab: results from the phase I KEYNOTE-001 study, J. Clin. Oncol. 37 (28) (2019) 2518–2527.
[5] A. Hamada, J. Soh, T. Mitsudomi, Salvage surgery after definitive chemoradiotherapy for patients with non-small cell lung cancer, Transl. Lung Cancer Res. 10 (1) (2021) 555–562.
[6] J.C. Simeone, B.L. Nordstrom, K. Patel, A.B. Klein, Treatment patterns and overall survival in metastatic non-small-cell lung cancer in a real-world, US setting, Future Oncol. 15 (30) (2019) 3491–3502.
[7] Y. An, H. Duan, The role of m6A RNA methylation in cancer metabolism, Mol. Cancer 21 (1) (2022) 14.
[8] S.K. Azzam, H. Alsafar, A.A. Sajini, FTO m6A demethylase in obesity and cancer: implications and underlying molecular mechanisms, Int. J. Mol. Sci. 23 (7) (2022) 3800.
[9] R. Wu, et al., m6A methylation promotes white-to-beige fat transition by facilitating Hif1a translation, EMBO Rep. 22 (11) (2021) e52348.
[10] L. Li, N. Xu, J. Liu, Z. Chen, X. Liu, J. Wang, m6A methylation in cardiovascular diseases: from mechanisms to therapeutic potential, Front. Genet. 13 (2022) 908976.
[11] R. Kumari, et al., mRNA modifications in cardiovascular biology and disease: with a focus on m6A modification, Cardiovasc. Res. 118 (7) (2022) 1680–1692.
[12] M. Han, et al., Abnormality of m6A mRNA methylation is involved in alzheimer's disease, Front. Neurosci. 14 (2020) 98.
[13] X. Chen, et al., Current insights into the implications of m6A RNA methylation and autophagy interaction in human diseases, Cell Biosci. 11 (1) (2021) 147.
[14] S. Zaccara, R.J. Ries, S.R. Jaffrey, Reading, writing and erasing mRNA methylation, Nat. Rev. Mol. Cell Biol. 20 (10) (2019) 608–624.
[15] X.Y. Chen, J. Zhang, J.S. Zhu, The role of m(6)A RNA methylation in human cancer, Mol. Cancer 18 (1) (2019) 103.
[16] J. Liu, D. Ren, Z. Du, H. Wang, H. Zhang, Y. Jin, m(6)A demethylase FTO facilitates tumor progression in lung squamous cell carcinoma by regulating MZF1 expression, Biochem. Biophys. Res. Commun. 502 (4) (2018) 456–464.
[17] Y. Ding, et al., FTO facilitates lung adenocarcinoma cell progression by activating cell migration through mRNA demethylation, OncoTargets Ther. 13 (2020) 1461–1470.
[18] J. Li, et al., The m6A demethylase FTO promotes the growth of lung cancer cells by regulating the m6A level of USP7 mRNA, Biochem. Biophys. Res. Commun. 512 (3) (2019) 479–485.
[19] N. Ishimwe, W. Zhang, J. Qian, Y. Zhang, L. Wen, Autophagy regulation as a promising approach for improving cancer immunotherapy, Cancer Lett. 475 (2020) 34–42.
[20] X. Li, S. He, B. Ma, Autophagy and autophagy-related proteins in cancer, Mol. Cancer 19 (1) (2020) 12.
[21] T. Marsh, J. Debnath, Autophagy suppresses breast cancer metastasis by degrading NBR1, Autophagy 16 (6) (2020) 1164–1165.
[22] K. Wang, et al., Synergistic chemopreventive effects of curcumin and berberine on human breast cancer cells through induction of apoptosis and autophagic cell death, Sci. Rep. 6 (2016) 26064.
[23] F. Wang, et al., N6-methyladenosine demethyltransferase FTO-mediated autophagy in malignant development of oral squamous cell carcinoma, Oncogene 40 (22) (2021) 3885–3898.
[24] Y. Xu, et al., FTO-mediated autophagy promotes progression of clear cell renal cell carcinoma via regulating SIK2 mRNA stability, Int. J. Biol. Sci. 18 (15) (2022) 5943–5962.
[25] P. Gulati, et al., Role for the obesity-related FTO gene in the cellular sensing of amino acids, Proc. Natl. Acad. Sci. U. S. A. 110 (7) (2013) 2557–2562.
[26] S. Jin, et al., m(6)A RNA modification controls autophagy through upregulating ULK1 protein abundance, Cell Res. 28 (9) (2018) 955–957.
[27] X. Wang, et al., m(6)A mRNA methylation controls autophagy and adipogenesis by targeting Atg5 and Atg7, Autophagy 16 (7) (2020) 1221–1235.
[28] J. He, et al., Antiviral potential of small molecules cordycepin, thymoquinone, and N6, N6-dimethyladenosine targeting SARS-CoV-2 entry protein ADAM17, Molecules 27 (24) (2022) 9044.
[29] Z. Han, et al., Crystal structure of the FTO protein reveals basis for its substrate specificity, Nature 464 (7292) (2010) 1205–1209.
[30] K. Wang, Y. Tu, J.B. Wan, M. Chen, C. He, Synergistic anti-breast cancer effect of pulsatilla saponin D and camptothecin through interrupting autophagic-lysosomal function and promoting p62-mediated ubiquitinated protein aggregation, Carcinogenesis 41 (6) (2020) 804–816.
[31] T. Ueno, M. Komatsu, Monitoring autophagy flux and activity: principles and applications, Bioessays 42 (11) (2020) e2000122.
[32] B. Cheng, et al., Profiling of RNA N (6) -methyladenosine methylation reveals the critical role of m(6)A in chicken adipose deposition, Front. Cell Dev. Biol. 9 (2021) 590468.
[33] X. Lin, et al., RNA m(6)A methylation regulates the epithelial mesenchymal transition of cancer cells and translation of Snail, Nat. Commun. 10 (1) (2019) 2065.
[34] H. Mu, et al., RNA binding protein IGF2BP1 meditates oxidative stress-induced granulosa cell dysfunction by regulating MDM2 mRNA stability in an m(6)A-dependent manner, Redox Biol. 57 (2022) 102492.
[35] K. Wang, et al., Role of the epigenetic modifier JMJD6 in tumor development and regulation of immune response, Front. Immunol. 13 (2022) 859893.
[36] N. Hariharan, P. Zhai, J. Sadoshima, Oxidative stress stimulates autophagic flux during ischemia/reperfusion, Antioxidants Redox Signal. 14 (11) (2011) 2179–2190.
[37] Y.T. Wu, et al., Dual role of 3-methyladenine in modulation of autophagy via different temporal patterns of inhibition on class I and III phosphoinositide 3-kinase, J. Biol. Chem. 285 (14) (2010) 10850–10861.
[38] Q. Li, et al., HIF-1alpha-induced expression of m6A reader YTHDF1 drives hypoxia-induced autophagy and malignancy of hepatocellular carcinoma by promoting ATG2A and ATG14 translation, Signal transduction and targeted therapy 6 (1) (2021) 76.
[39] W. Wang, et al., m(6)A RNA demethylase FTO promotes the growth, migration and invasion of pancreatic cancer cells through inhibiting TFPI-2, Epigenetics 17 (12) (2022) 1738–1752.
[40] Y. Chen, et al., The functions and roles of sestrins in regulating human diseases, Cell. Mol. Biol. Lett. 27 (1) (2022) 2.
[41] C. Lu, Y. Jiang, W. Xu, X. Bao, Sestrin2: multifaceted functions, molecular basis, and its implications in liver diseases, Cell Death Dis. 14 (2) (2023) 160.
[42] F. Peng, et al., Oncogenic AURKA-enhanced N(6)-methyladenosine modification increases DROSHA mRNA stability to transactivate STC1 in breast cancer stem-like cells, Cell Res. 31 (3) (2021) 345–361.
[43] H. Huang, et al., Recognition of RNA N(6)-methyladenosine by IGF2BP proteins enhances mRNA stability and translation, Nat. Cell Biol. 20 (3) (2018) 285–295.
[44] J. Huang, et al., FTO suppresses glycolysis and growth of papillary thyroid cancer via decreasing stability of APOE mRNA in an N6-methyladenosine-dependent manner, J. Exp. Clin. Cancer Res. 41 (1) (2022) 42.
[45] L. Zhang, et al., IGF2BP1 overexpression stabilizes PEG10 mRNA in an m6A-dependent manner and promotes endometrial cancer progression, Theranostics 11 (3) (2021) 1100–1114.

[46] L. Liu, et al., The N6-methyladenosine modification enhances ferroptosis resistance through inhibiting SLC7A11 mRNA deadenylation in hepatoblastoma, Clin. Transl. Med. 12 (5) (2022) e778.
[47] Y.H. Cui, et al., Autophagy of the m(6)A mRNA demethylase FTO is impaired by low-level arsenic exposure to promote tumorigenesis, Nat. Commun. 12 (1) (2021) 2183.
[48] B. You, et al., AMPK-mTOR-Mediated activation of autophagy promotes formation of dormant polyploid giant cancer cells, Cancer Res. 82 (5) (2022) 846–858.
[49] T. Sanli, K. Linher-Melville, T. Tsakiridis, G. Singh, Sestrin2 modulates AMPK subunit expression and its response to ionizing radiation in breast cancer cells, PLoS One 7 (2) (2012) e32035.
[50] G.J. Yoshida, Therapeutic strategies of drug repositioning targeting autophagy to induce cancer cell death: from pathophysiology to treatment, J. Hematol. Oncol. 10 (1) (2017) 67.
[51] T. Johansen, T. Lamark, Selective autophagy mediated by autophagic adapter proteins, Autophagy 7 (3) (2011) 279–296.
[52] N. Meyer, et al., Autophagy activation, lipotoxicity and lysosomal membrane permeabilization synergize to promote pimozide- and loperamide-induced glioma cell death, Autophagy 17 (11) (2021) 3424–3443.
[53] J.G. Yoo, Y.K. Lee, K.H. Lee, Enhancing autophagy leads to increased cell death in radiation-treated cervical cancer cells, J. Obstet. Gynaecol. 43 (1) (2023) 2171281.
[54] M. De Santi, G. Baldelli, A. Diotallevi, L. Galluzzi, G.F. Schiavano, G. Brandi, Metformin prevents cell tumorigenesis through autophagy-related cell death, Sci. Rep. 9 (1) (2019) 66.
[55] C.F. Song, et al., Hernandezine induces autophagic cell death in human pancreatic cancer cells via activation of the ROS/AMPK signaling pathway, Acta Pharmacol. Sin. 44 (4) (2023) 865–876.
[56] Y. Wang, S. Wang, J. Xu, Y. Wang, L. Xiang, X. He, Total steroidal saponins from black nightshade (Solanum nigrum L.) overcome tumor multidrug resistance by inducing autophagy-mediated cell death in vivo and in vitro, Phytother Res. 37 (7) (2023) 3009–3024.
[57] Y. Liang, et al., Cadmium promotes breast cancer cell proliferation, migration and invasion by inhibiting ACSS2/ATG5-mediated autophagy, Environ. Pollut. 273 (2021) 116504.
[58] Z. Li, et al., FTO plays an oncogenic role in acute myeloid leukemia as a N(6)-methyladenosine RNA demethylase, Cancer Cell 31 (1) (2017) 127–141.
[59] Y. Niu, et al., RNA N6-methyladenosine demethylase FTO promotes breast tumor progression through inhibiting BNIP3, Mol. Cancer 18 (1) (2019) 46.
[60] X. Bian, et al., AMD1 upregulates hepatocellular carcinoma cells stemness by FTO mediated mRNA demethylation, Clin. Transl. Med. 11 (3) (2021) e352.
[61] S. Yang, et al., m(6)A mRNA demethylase FTO regulates melanoma tumorigenicity and response to anti-PD-1 blockade, Nat. Commun. 10 (1) (2019) 2782.
[62] L. Zhao, X. Kong, W. Zhong, Y. Wang, P. Li, FTO accelerates ovarian cancer cell growth by promoting proliferation, inhibiting apoptosis, and activating autophagy, Pathol. Res. Pract. 216 (9) (2020) 153042.
[63] Y. Zhang, L.X. Gao, W. Wang, T. Zhang, F.Y. Dong, W.P. Ding, M(6) A demethylase fat mass and obesity-associated protein regulates cisplatin resistance of gastric cancer by modulating autophagy activation through ULK1, Cancer Sci. 113 (9) (2022) 3085–3096.
[64] S. Feng, et al., Omeprazole improves chemosensitivity of gastric cancer cells by m6A demethylase FTO-mediated activation of mTORC1 and DDIT3 up-regulation, Biosci. Rep. 41 (1) (2021) BSR20200842.
[65] I. Tsilioni, A.S. Filippidis, T. Kerenidi, A.V. Budanov, S.G. Zarogiannis, K.I. Gourgoulianis, Sestrin-2 is significantly increased in malignant pleural effusions due to lung cancer and is potentially secreted by pleural mesothelial cells, Clin. Biochem. 49 (9) (2016) 726–728.
[66] H. Xu, et al., An ShRNA based Genetic screen identified Sesn2 as a potential tumor suppressor in lung cancer via suppression of Akt-mTOR-p70S6K signaling, PLoS One 10 (5) (2015) e0124033.
[67] Y.L. Wang, Q. Wang, H. Li, C.C. Wang, Y.L. Ma, Z. Han, Sestrin2 mediates FOXM1 expression to block the EMT process in non-small cell lung cancer through the AMPK/YAP pathway, Neoplasma 70 (1) (2023) 46–57.
[68] Y. Liang, et al., SESN2/sestrin 2 induction-mediated autophagy and inhibitory effect of isorhapontigenin (ISO) on human bladder cancers, Autophagy 12 (8) (2016) 1229–1239.